CHEMISTRY OF MATERIALS
Article

Chem. Mater. **2011,** *23,* 851–861 851
DOI:10.1021/cm1021867

Electron-Withdrawing Substituted Tetrathiafulvalenes as Ambipolar Semiconductors†

Francisco Otón,‡ Raphael Pfattner,‡ Egon Pavlica,§ Yoann Olivier,∥ Evelyn Moreno,‡ Joaquim Puigdollers,⊥ Gvido Bratina,§ Jérôme Cornil,∥ Xavier Fontrodona,# Marta Mas-Torrent,*,‡ Jaume Veciana,‡ and Concepció Rovira*,‡

‡*Institut de Ciència de Materials de Barcelona* (*CSIC*) *and Networking Research Center on Bioengineering, Biomaterials and Nanomedicine* (*CIBER-BBN*), *Campus Universitari de Bellaterra, Cerdanyola E-08193, Barcelona, Spain,* §*Laboratory for Organic Matter Physics, University of Nova Gorica, Vipavska 13, SI-5000 Nova Gorica, Slovenia,* ∥*Laboratory for Chemistry of Novel Materials, University of Mons, Place du Parc 20, B-7000 Mons, Belgium,* ⊥*Department of Eng. Electronica and CrNE, Universitat Politecnica Catalunya, E-08034 Barcelona, Spain, and* #*Serveis Tecnics de Recerca, Universitat de Girona, Edifici Jaume Casademont* (*porta E*), *Pic de Peguera, 15 La Creueta, E-17003 Girona, Spain*

Received August 2, 2010. Revised Manuscript Received September 22, 2010

The synthesis of four new TTF derivatives bearing phthalimides and fluorinated alkyl moieties as potential ambipolar semiconductors is described. The presence of such electron-withdrawing groups permits the stabilization of the energy of HOMO and LUMO orbitals. The solid-state structures of these novel molecules have been characterized by X-ray diffraction techniques. The potential of these materials as hole and electron conductors has been estimated under theoretical considerations by evaluating the position of the frontier energy levels as well as their charge carrier mobilities. Preparation of solution-processed single crystal organic field-effect transistors (OFETs) has resulted in hole mobilities of up to 0.33 $cm^2\ V^{-1}\ s^{-1}$ for compound **1**. On the other hand, electrical time of flight (EToF) measurements on single crystals of compound **3** demonstrated ambipolar transport, reaching very high mobility values around 2.0 $cm^2\ V^{-1}\ s^{-1}$ for both types of charges.

Introduction

The advances in the electronic performance of organic devices in the past few years have attracted a great interest not only from the academic world but also from large international companies.[1,2] Up to now, the performance of the electro-active organic semiconductor is still the most important component to be optimized to obtain efficient devices. The ideal material should be preferentially solution processable, long-term stable, and cheap to synthesize, in addition to exhibit a high charge transport mobility. Indeed, for practical device applications such as solar cells, organic light-emitting diodes (OLEDs), or organic field effect transistors (OFETs), materials with mobilities higher than 1 $cm^2\ V^{-1}\ s^{-1}$ are required.[1,2] However, the understanding of the processes that govern charge carrier mobility is still not clear, and thus, the prediction of the transport characteristics of a new material is nowadays a huge challenge. In this sense, the characterization of single crystal OFETs allows the intrinsic mechanisms of charge transport in the absence of grain boundaries or defects that tend to decrease the charge carrier mobility to be studied, making the characterization of the semiconductor itself less uncertain.[3,4] Understanding the relationship between molecular structure and transport properties of a material is a key point for providing guidelines for device design, and a great research effort is being made in this direction.[2,3,5−7] Other challenges which are probably the most important in the design of new semiconductors are the understanding of the relationship between chemical structure and crystal packing as well as crystal packing and charge carrier mobility.[8] Some progress has been made recently in the development of methods to predict the crystal structure from the chemical structure,[9] but this procedure is still difficult to apply systematically.

Several compounds of the family of tetrathiafulvalenes (TTFs) have been demonstrated to behave as high mobility semiconductors in OFETs.[10] The highest mobilities in TTF OFETs, which are among the largest values reported for OFETs, have been found for single crystals prepared

† Accepted as part of the "Special Issue on π-Functional Materials".

*To whom correspondence should be addressed. E-mail: cun@icmab.es, mmas@icmab.es. Fax: (+34) 935805729.

(1) Arias, A. C.; MacKenzie, J. D.; McCulloch, I.; Rivnay, J.; Salleo, A. *Chem. Rev.* **2010**, *110*, 3–24.
(2) Wu, W.; Liu, Y.; Zhu, D. *Chem. Soc. Rev.* **2010**, *39*, 1489–1502.
(3) Rivnay, J.; Jimison, L. H.; Northrup, J. E.; Toney, M. F.; Noriega, R.; Lu, S.; Marks, T. J.; Facchetti, A. *Nat. Mater.* **2009**, *8*, 952–958.
(4) Tang, Q.; Jiang, L.; Tong, Y.; Li, H.; Liu, Y.; Wang, Z.; Hu, W.; Liu, Y.; Zhu, D. *Adv. Mater.* **2008**, *20*, 2947–2951.
(5) Liu, C.; Liu, Z.; Lemke, H. T.; Tsao, H. N.; Naber, R. C. G.; Li, Y.; Banger, K.; Müllen, K.; Nielsen, M. M.; Sirringhaus, H. *Chem. Mater.* **2010**, *22*, 2120–2124.
(6) Letizia, J. A.; Cronin, S.; Ortiz, R. P.; Facchetti, A.; Ratner, M. A.; Marks, T. J. *Chem.—Eur. J.* **2010**, *16*, 1911–1928.
(7) Coropceanu, V.; Cornil, J.; da Silva Filho, D. A.; Olivier, Y.; Silbey, R.; Brédas, J. L. *Chem. Rev.* **2007**, *107*, 926–952.
(8) Delgado, R. F. R.; Kim, E.-G.; Filho, D. A. d. S.; Bredas, J.-L. *J. Am. Chem. Soc.* **2010**, *132*, 3375–3387.

Published on Web 10/21/2010

from solution of dithiophene-tetrathiafulvalene (DT-TTF, μ_{max} = 3.6 $cm^2\ V^{-1}\ s^{-1}$),[11] hexamethylene-tetrathiafulvalene (HM-TTF, μ_{max} = 10 $cm^2\ V^{-1}\ s^{-1}$),[12−14] dibenzotetrathiafulvalene (DB-TTF, μ_{max} = 1 $cm^2\ V^{-1}\ s^{-1}$),[15] and a parent TTF compound (μ_{max} = 1.2 $cm^2\ V^{-1}\ s^{-1}$).[16] Due to the strong donor character of these molecules, in most of the reported devices the TTF analogues behave as p-type semiconductors (i.e., hole conduction), with the exception of only two TTF derivatives with strong electron-withdrawing substituents that have been shown to behave as n-type semiconductors (i.e., electron conduction).[17] N-type and ambipolar (i.e., hole and electron conduction) semiconductors are of special importance for the fabrication of p-n junctions and complementary circuits.[18−24] However, despite the intense work devoted to the development of these materials, their performance is still far from the one found with p-type organic semiconductors. This can be partly caused by electron trapping in ambient air and/or at the dielectric surface sites but also by the lack of stable materials. Another major issue to achieve electron conduction is the electron injection. Indeed, organic semiconductors should have LUMO energy levels which match the work function of the source−drain electrodes to decrease the electron injection barrier, a value that is commonly assumed to be lower than −4.0 eV.[25] Similarly, hole conduction is ensured when the materials have a HOMO level aligned with the work function of the hole injecting electrode. Therefore, one approach to preparing ambipolar organic semiconductors is to introduce electron acceptor units to the molecular cores of well-known p-type semiconductors such as oligothiophenes, acenes or tetrathiafulvalenes.[19−24] Moreover, the presence of electron-withdrawing groups, such as phthalimides, among others,[26] leads to the decrease of both the HOMO and LUMO energy levels that is known to improve the air stability and reliability of the prepared devices.[27−29]

In this paper we report the synthesis of four new *bis*-phthalimide substituted TTF derivatives as novel ambipolar semiconductors. The electron-withdrawing groups attached to the TTF molecule increase the electron affinity of the materials but keep the HOMO energies sufficiently unaltered to guarantee hole injection.[26] These materials were fully characterized in solution as well as in solid state. Also, a careful theoretical investigation was carried out to study the potential of these materials for charge transport in terms of energy levels and crystal packing. Single crystal OFETs were fabricated, achieving a maximum hole mobility of 0.33 $cm^2\ V^{-1}\ s^{-1}$. Furthermore, the charge carrier mobility of the materials was also investigated by electrical time of flight (EToF) and hole, and electron mobilities as high as 2.0 $cm^2\ V^{-1}\ s^{-1}$ have been found for some of the materials.

Experimental Section

Materials and Methods. All reactions were carried out under Ar using solvents which were dried following routine procedures. *Bis*-(bromomethyl)dithiolone[30] was synthesized using procedures reported in the literature. Graphite paste XC-12 was purchased from Dotite, and thermally grown silicon dioxide was purchased from Si-Mat. Chemical reagents obtained from commercial sources were used without further purification. Column chromatography was performed using silica gel (60 A C.C. 35−70 μm, sds) as the stationary phase. The MALDI-TOF MS spectra were recorded on a Bruker Ultraflex II TOF spectrometer. Infrared spectra were recorded on a Perkin-Elmer FT-IR Spectrum One spectrophotometer. UV−vis spectra were performed in *o*-dichlorobenzene heated at 100 °C ($c = 1 \times 10^{-4}$ M) using a VARIAN CARY 5000 spectrophotometer. Elemental analyses were carried out on a Carlo Erba CE 1108 elemental analyzer. Cyclic voltammograms (CV) were performed with a conventional three-electrode configuration consisting of platinum wires as working and auxiliary electrodes and Ag as pseudoreference electrode. These experiments were carried out in a 10^{-3} M solution of the corresponding TTF derivative in *o*-dichlorobenzene, thermostatted at 150 °C to be able to solubilize the materials, and containing 0.1 M of (n-$C_4H_9)_4PF_6$ (TBAHP) as supporting electrolyte. Deoxygenation of the solutions was performed previously to the experiments by bubbling nitrogen for at least 10 min, and the working electrode was cleaned after each run. The CVs were recorded with an increasing scan rate from 0.05 to 0.50 V s^{-1}. Ferrocene was used as an internal reference both for potential calibration and for

(9) Day, G. M.; Cooper, T. G.; Cruz-Cabeza, A. J.; Hejczyk, K. E.; Ammon, H. L.; Boerrigter, S. X. M.; Tan, J. S.; Della Valle, R. G.; Venuti, E.; Jose, J.; Gadre, S. R.; Desiraju, G. R.; Thakur, T. S.; van Eijck, B. P.; Facelli, J. C.; Bazterra, V. E.; Ferraro, M. B.; Hofmann, D. W. M.; Neumann, M. A.; Leusen, F. J. J.; Kendrick, J.; Price, S. L.; Misquitta, A. J.; Karamertzanis, P. G.; Welch, G. W. A.; Scheraga, H. A.; Arnautova, Y. A.; Schmidt, M. U.; van de Streek, J.; K., W. A.; B., S. *Acta Crystallogr., Sect. B* **2009**, *65*, 107–125.
(10) Mas-Torrent, M.; Rovira, C. *J. Mater. Chem.* **2006**, *16*, 433–436.
(11) Leufgen, M.; Rost, O.; Gould, C.; Schmidt, G.; Geurts, J.; Molenkamp, L. W.; Oxtoby, N. S.; Mas-Torrent, M.; Crivillers, N.; Veciana, J.; Rovira, C. *Org. Electron.* **2008**, *9*, 1101–1106.
(12) Takahashi, Y.; Hasegawa, T.; Horiuchi, S.; Kumai, R.; Tokura, Y.; Saito, G. *Chem. Mater.* **2007**, *19*, 6382–6384.
(13) Kanno, M.; Bando, Y.; Shirahata, T.; Inoue, J.-I.; Wada, H.; Mori, T. *J .Mater. Chem.* **2009**, *19*, 6548–6555.
(14) Yamada, T.; Kumai, R.; Takahashi, Y.; Hasegawa, T. *J. Mater. Chem.* **2010**, *20*, 5810–5812.
(15) Mas-Torrent, M.; Hadley, P.; Bromley, S. T.; Crivillers, N.; Veciana, J.; Rovira, C. *Appl. Phys. Lett.* **2005**, *86*, 012110/1–3.
(16) Jiang, H.; Yang, X.; Cui, Z.; Liu, Y.; Li, H.; Hu, W.; Liu, Y.; Zhu, D. *Appl. Phys. Lett.* **2007**, *91*, 123505.
(17) Naraso; Nishida, J.-i.; Kumaki, D.; Tokito, S.; Yamashita, Y. *J. Am. Chem. Soc.* **2006**, *128*, 9598–9599.
(18) Mas-Torrent, M.; Rovira, C. *Chem. Soc. Rev.* **2008**, *37*, 827–838.
(19) Jones, B. A.; Facchetti, A.; Wasielewski, M. R.; Marks, T. J. *J. Am. Chem. Soc.* **2007**, *129*, 15259–15278.
(20) Wang, Z.; Kim, C.; Facchetti, A.; Marks, T. J. *J. Am. Chem. Soc.* **2007**, *129*, 13362–13363.
(21) Mamada, M.; Nishida, J.; Kumaki, D.; Tokito, S.; Yamashita, Y. *Chem. Mater.* **2007**, *19*, 5404–5409.
(22) Tang, M. L.; Reichardt, A. D.; Miyaki, N.; Stoltenberg, R. M.; Bao, Z. *J. Am. Chem. Soc.* **2008**, *130*(19), 6064–6065.
(23) Sakamoto, Y.; Suzuki, T.; Kobayashi, M.; Gao, Y.; Y., F.; Inoue, Y.; Sato, F.; Tokito, S. *J. Am. Chem. Soc.* **2004**, *126*, 8138–8140.
(24) Mushrush, M.; Facchetti, A.; Lefenfeld, M.; Katz, H. E.; Marks, T. J. *J. Am. Chem. Soc.* **2003**, *125*, 9414–9423.
(25) Newman, C. R.; Frisbie, C. D.; da Silva, D. A.; Bredas, J. L.; Ewbank, P. C.; Mann, K. R. *Chem. Mater.* **2004**, *16*, 4436–4451.
(26) Gao, X.; Wang, Y.; Yang, X.; Liu, Y.; Qiu, W.; Wu, W.; Zhang, H.; Qi, T.; Liu, Y.; Lu, K.; Du, C.; Shuai, Z.; Yu, G.; Zhu, D. *Adv. Mater.* **2007**, *19*, 3037–3042.
(27) Ie, Y.; Nitani, M.; Karakawa, M.; Tada, H.; Aso, Y. *Adv. Funct. Mater.* **2010**, *20*, 907–913.
(28) Salman, S.; Ruiz-Delgado, M. C.; Coropceanu, V.; Bredas, J.-L. *Chem. Mater.* **2009**, *21*, 3593–3601.
(29) Yoon, M.-H.; DiBenedetto, S. A.; Russell, M. T.; Facchetti, A.; Marks, T. J. *Chem. Mater.* **2007**, *19*, 4864–4881.
(30) Crivillers, N.; Oxtoby, N. S.; Mas-Torrent, M.; Veciana, J.; Rovira, C. *Synthesis* **2007**, *11*, 1621–1623.

reversibility criteria. All of the potential values reported are relative to the Fc^+/Fc couple at room temperature. Under these conditions ferrocene has a redox potential of $E^0 = 0.440$ V vs Ag/AgCl saturated electrode, and the anodic−cathodic peak separation is 67 mV. Crystallographic data of **1** and **3** were measured in a Bruker SMART Apex CCD using graphite-monochromated Mo Kα radiation ($\lambda = 0.71073$ Å) from an X-ray tube. The measurements were made in the range 2.44 to 28.22° for θ. Full-sphere data collection was carried out with φ and ω scans. Programs used: data collection, Smart version 5.631 (Bruker AXS 1997-02); data reduction, Saint + version 6.36A (Bruker AXS 2001); absorption correction, SADABS version 2.10 (Bruker AXS 2001). Structure solution and refinement was done by using SHELXTL Version 6.14 (Bruker AXS 2000−2003). The structure was solved by direct methods and refined by full-matrix least-squares methods on F^2. The non-hydrogen atoms were refined anisotropically. The H-atoms were placed in geometrically optimized positions and forced to ride on the atom to which they are attached.

Polycrystalline samples of **2** and **4** were measured in a Panalytical X'Pert Pro MPD diffractometer equipped with a θ/θ goniometer of 240 mm of radii. The diffractometer was used in a capillarity transmission geometry with a elliptic focusing mirror in the incident beam, enabling the selection of the Cu (Kα1 + 2) radiation ($\lambda = 1.54118$ Å) and a PIXCel detector. Strictly monophasic samples of **2** and **4** were gently ground in an agate mortar and then loaded into 0.5 mm diameter Lindemann glass capillaries. The capillary rotates around its axis during 13 h over the range 2.0−70.0° (2θ). Standard peak search methods, followed by indexing with X-Cell[31] algorithm available in the PC modeling platform Material Studio (Materials Studio Modeling 4.2.; Information available at http://accelrys.com/products/materials-studio) allowed the determination of the approximate cell parameters. Systematic absences, where pertinent, and density considerations clearly indicated the corresponding space group, later confirmed by successful structure solution and refinement. The geometries of the substituent R of compounds **2** and **4** were optimized by means of a force field geometry optimization using the COMPASS[32] force field. Structure solution was initiated by employing a semirigid molecular fragment flexible about the C−N−C−C torsion angle such as to allow the R substituent to freely rotate with respect to the fixed planar geometry of the TTF skeleton (information taken from the known single-crystal structures of **1** and **3**) placed at (0,0,0) and (1/2,1/2,1/2) spatial positions that was allowed to rotate. Direct-space methods following a Monte Carlo simulated annealing[33] allowed the orientation of the used fragments to be determined and later refined by the Rietveld method.[34,35] The final structure is obtained by alternated cycles of Rietveld refinement followed by geometry optimization using the COMPASS force field. This sequence is performed several times to provide a structure that both is chemically stable and gives the best agreement with the experimental powder pattern. In the Rietveld procedure, the fundamental parameter approach in describing the peak shapes was employed, the background contribution was modeled by a polynomial fit, and preferred orientation effects were described by the March-Dollase model[36] (001 pole). A single isotropic thermal parameter was adopted for all atoms. Crystal data and details of the structural analysis, including those for the two phases characterized by single-crystal X-ray diffraction, are reported in Table S1 (see Supporting Information).

Electrical ToF measurements were performed in the following way:[37] The source electrode was connected to a low impedance ammeter, which was used to measure source current. The drain electrode was connected to a voltage source, which can measure also drain current. Gate voltage was applied to the n-doped Si substrate, which served as the gate electrode. During the measurement of the drain and source current, the drain voltage was changing in a cyclic way, and the gate voltage was kept constant. The difference between the source and the drain current was used to roughly estimate the leakage current. For more details see Supporting Information. OFETs were fabricated on 200 nm thermally oxidized silicon substrates. Crystals were formed on the substrate by drop casting a solution of 0.5−1.0 mg of the compounds in 1 mL of toluene or chlorobenzene and allowing the solvent to evaporate slowly under darkness and reduced ambient humidity. The prepared devices were measured in a Süss Microtech Probe Station EP4 equipped with micromanipulators and with a two-channel Keithley SourceMeter 2612. Graphite paste used as source and drain electrodes was applied on the mounted crystals with a small brush and dried in air.

Computational Details. Geometries were fully optimized with tight convergence criteria at the density functional theory (DFT) level with the Gaussian 09 package (A02 release),[38] using the B3LYP[39] functional and the 6-31G(d,p) basis set. All energies are not corrected for the zero-point vibrational energy. The electronic structures and the reorganization energies were calculated at the same level of theory. Transfer integrals have been calculated at the DFT level with the B3LYP functional and TZP basis set, using the fragment approach implemented in the ADF package with the methodology described in refs 40 and 41. Internal reorganization energies were calculated with B3LYP functional and 6-31G(d,p) basis set.

General Procedure for the Synthesis of the Bisphthalimide-TTF Derivatives. A solution of the corresponding thione[42]

(31) Neumann, M. A. *J. Appl. Crystallogr.* **2003**, *36*, 356–365.
(32) Sun, H. *J. Phys. Chem. A* **1998**, *102*, 7338–7364.
(33) Tremayne, M.; Kariuki, B. M.; Harris, K. D. M. *J. Appl. Crystallogr.* **1996**, *29*, 211–214.
(34) Young, R. A. *The Rietveld Method*; Oxford University Press: Oxford, 1995.
(35) McCusker, L. B.; Dreele, R. B. V.; Cox, D. E.; Louer, D.; Scardi, P. *J. Appl. Crystallogr.* **1999**, *32*, 36–50.
(36) Dollase, W. A. *J. Appl. Crystallogr.* **1986**, *19*, 267–272.
(37) Dunn, L.; Basu, D.; Wang, L.; Dodabalapur, A. *Appl. Phys. Lett.* **2006**, *88*, 063507.
(38) Frisch, M. J.; Trucks, G. W.; Schlegel, H. B.; Scuseria, G. E.; Robb, M. A.; Cheeseman, J. R.; Scalmani, G.; Barone, V.; Mennucci, B.; Petersson, G. A.; Nakatsuji, H.; Caricato, M.; Li, X.; Hratchian, H. P.; Izmaylov, A. F.; Bloino, J.; Zheng, G.; Sonnenberg, J. L.; Hada, M.; Ehara, M.; Toyota, K.; Fukuda, R.; Hasegawa, J.; Ishida, M.; Nakajima, T.; Honda, Y.; Kitao, O.; Nakai, H.; Vreven, T.; Montgomery, J. A., Jr.; Peralta, J. E.; Ogliaro, F.; Bearpark, M.; Heyd, J. J.; Brothers, E.; Kudin, K. N.; Staroverov, V. N.; Kobayashi, R.; Normand, J.; Raghavachari, K.; Rendell, A.; Burant, J. C.; Iyengar, S. S.; Tomasi, J.; Cossi, M.; Rega, N.; Millam, N. J.; Klene, M.; Knox, J. E.; Cross, J. B.; Bakken, V.; Adamo, C.; Jaramillo, J.; Gomperts, R.; Stratmann, R. E.; Yazyev, O.; Austin, A. J.; Cammi, R.; Pomelli, C.; Ochterski, J. W.; Martin, R. L.; Morokuma, K.; Zakrzewski, V. G.; Voth, G. A.; Salvador, P.; Dannenberg, J. J.; Dapprich, S.; Daniels, A. D.; Farkas, Ö.; Foresman, J. B.; Ortiz, J. V.; Cioslowski, J.; Fox, D. J. *Gaussian 09*, Revision A.1; Gaussian, Inc.: Wallingford, CT, 2009.
(39) Bartolottiand, L. J.; Fluchick, K. *Reviews in Computational Chemistry*; VCH: New York, 1996; Vol. *7*.
(40) Valeev, E. F.; Coropceanu, V.; Silva, D. A. d.; Salman, S.; Brédas, J.-L. *J. Am. Chem. Soc.* **2006**, *128*, 9882–9886.
(41) Senthilkumar, K.; Grozema, F. C.; Bickelhaupt, F. M.; Siebbeles, L. D. A. *J. Chem. Phys.* **2003**, *119*, 9809–9817.
(42) Otón, F.; Pfattner, R.; Oxtoby, N. S.; Mas-Torrent, M.; Wurst, K.; Fontrodona, X.; Olivier, Y.; Cornil, J.; Veciana, J.; Rovira, C. Submitted.

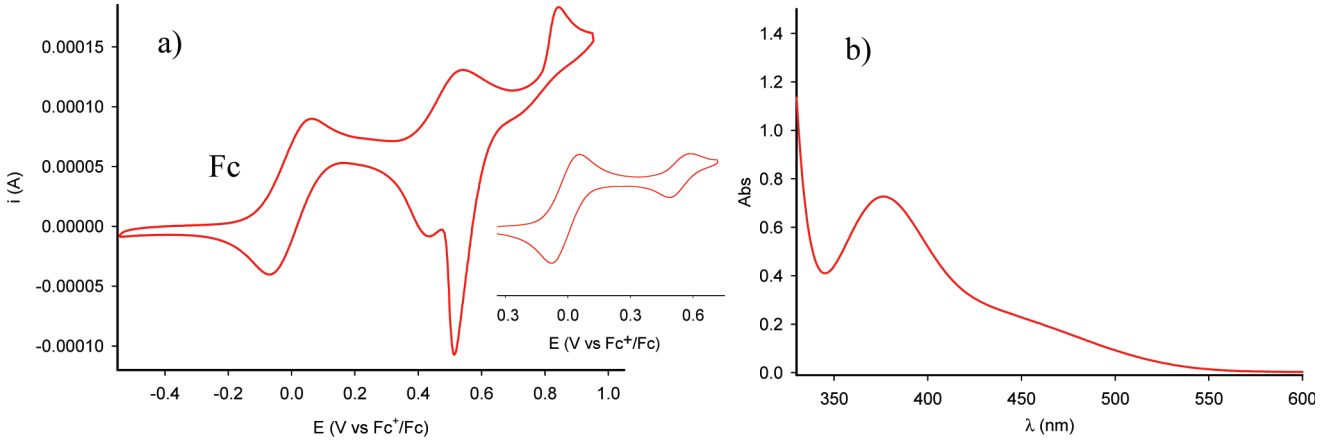

Figure 1. (a) Cyclic voltammogram (inset: first oxidation wave) and (b) UV−vis spectrum of **1** in *o*-dichlorobenzene.

(0.538 mmol) in 10 mL of freshly distilled trimethylphosphite is refluxed in inert atmosphere for 8 h. After this time, the solution is left to cool down, and the solvent is removed. The humid red residue is dispersed in CH_2Cl_2 and filtered. The resulting red/orange solid is washed successively with 50 mL of water, MeOH, CH_3CN, THF, CH_2Cl_2, and Et_2O and dried in the filter to obtain the polycrystalline *bis*-imides with good purity.

Bis-(*N-propyl-phthalimido*[*5,6-d*])*tetrathiafulvalene, **1***. Yield = 85%. Mp > 350 °C. FT-IR (ATR): ν = 3084, 2974, 2934, 2881, 1767, 1750, 1705, 1593, 1463, 1436, 1391, 1367, 1322, 1312, 1204, 1191, 1054, 913, 875, 786, 742 cm^{-1}. MALDI-TOF-MS: m/z = 525.9 (M^+, 100%). Elem anal. Calcd (%) for $C_{24}H_{18}N_2O_4S_4$: C, 54.73; H, 3.44; N, 5.32; S, 24.35. Found: C, 54.76; H, 3.37; N, 5.30; S, 24.25.

Bis-(*N*-(*2,2,2-trifluoroethyl*)-*phthalimido*[*5,6-d*])*tetrathiafulvalene, **2***. Yield = 74%. Mp > 350 °C. FT-IR (ATR): ν = 3099, 2977, 1783, 1753, 1726, 1714, 1591, 1415, 1391, 1336, 1313, 1256, 1201, 1183, 1167, 1093, 1063, 916, 894, 881, 836, 747, 732 cm^{-1}. MALDI-TOF-MS: m/z = 605.9 (M^+, 100%). Elem anal. Calcd (%) for $C_{22}H_8F_6N_2O_4S_4$: C, 43.56; H, 1.33; N, 4.62; S, 21.15. Found: C, 43.60; H, 1.20; N, 4.53; S, 4.55.

Bis-(*N*-(*4,4,4,3,3,2,2-heptafluorobuthyl*)-*phthalimido*[*5,6-d*])-*tetrathiafulvalene, **3***. Yield = 56%. Mp > 350 °C. FT-IR (ATR): ν = 3090, 2964, 1784, 1750, 1715, 1590, 1417, 1398, 1384, 1356, 1342, 1311, 1228, 1198, 1169, 1122, 1103, 1062, 1001, 958, 916, 876, 794, 779 cm^{-1}. MALDI-TOF-MS: m/z = 806.3 (M^+, 100%). Elem anal. Calcd (%) for $C_{26}H_8F_{14}N_2O_4S_4$: C, 38.72; H, 1.00; N, 3.47; S, 15.90. Found: C, 38.85; H, 1.03; N, 3.48; S, 15.72.

Bis-(*N*-(*p-triflouromethylphenyl*)-*phthalimido*[*5,6-d*])*tetrathiafulvalene, **4***. Yield = 68%. Mp > 350 °C. FT-IR (ATR): ν = 3086, 1772, 1712, 1616, 1588, 1519, 1436, 1420, 1376, 1327, 1312, 1233, 1193, 1172, 1112, 1067, 1019, 948, 914, 875, 864, 836, 768, 737 cm^{-1}. MALDI-TOF-MS: m/z = 730.0 (M^+, 100%). Elem anal. Calcd (%) for $C_{32}H_{12}F_6N_2O_4S_4$: C, 52.60; H, 1.66; N, 3.83; S, 17.55. Found: C, 52.71; H, 1.73; N, 3.74; S, 17.39.

Results and Discussion

Synthesis. Reaction of *n*-alkyl and -aryl maleimides,[43] with 3,4-*bis*-(bromomethyl)dithiolthione[30] resulted in the formation of a group of phthalimide-fused dithiol-2-ones (see Supporting Information).[42] Further reaction in a reflux of freshly distilled trimethylphosphite led to the TTF derivatives **1**−**4** in yields that ranged from moderate to high. The identity and purity of the products were studied by the common spectroscopic techniques (FTIR, MS, and elemental analysis), and in some cases the nature of the compounds was confirmed by single crystal XRD. As a result of the low solubility of this family of compounds, NMR characterization could not be carried out.

Electrochemical and UV−Vis Characterization. The electrochemical properties of TTFs **1**−**4** were investigated by cyclic voltammetry (CV). Because of the low solubility of the compounds, the experiments were performed in *o*-dichlorobenzene thermostatted at 150 °C. Two oxidation processes were clearly observed at very similar half wave potentials in all cases (Figure 1 and Table 1). The first oxidation process for **2**, **3**, and **4** occurs around $E_{1/2}(1) = 0.55$ V (vs Fc^+/Fc), whereas for **1** the half wave potential is shifted 80 mV ($E_{1/2}(1)$ = 0.47 V) due to the lack of fluorine substituted side groups. The anodic peak of the second wave appears in the range E_p = 0.83−0.89 V (Table 1), where the most cathodically shifted values correspond to the fluorinated derivatives **3** and **4**. The reversibility of the first wave has been confirmed by applying a small voltage window (see inset Figure 1). However, when the oxidation window is enlarged to more anodic potentials to observe the second oxidation process, a clear striping process is observed in all compounds. This phenomenon can be attributed to the low solubility of the dioxidized species that creates a large overpotential. No reduction peaks were observed in the voltammogram because the baseline was too unstable above −1.5 V due to the experimental conditions used.

The UV−vis studies were also carried out in a hot solution (100 °C) of *o*-dichlorobenzene ($c = 10^{-4}$ M) to allow the complete solubilization of the samples. As expected, the UV−vis spectra of all compounds are quite similar due to the limited influence of the lateral chains in the values of HOMO and LUMO energies (vide infra). They show a band at λ = 380 nm for **1**, λ = 385 nm for **2**, **3**, and **4**, and a broad shoulder at λ = 445 nm for **1** and λ = 461 nm for the other members of the family (see Supporting Information).

(43) Reddy, P. Y.; Kondo, S.; Toru, T.; Ueno, Y. *J. Org. Chem.* **1997**, *62*(8), 2652–2654.

Table 1. Electrochemical Data and HOMO-LUMO Energy Levels Estimated Experimentally and Theoretically

			UV−vis/electrochem.[a]		DFT calculations[b]	
comp.	$E_{1/2Ox1}$ (V)	$E_{p(an)}/E_{p(cat)Ox2}$ (V)	HOMO	LUMO	HOMO (eV)	LUMO (eV)
1	0.47	0.83/0.52	−5.27	−3.01	−5.34	−2.45
2	0.54	0.88/0.55	−5.34	−3.15	−5.56	−2.73
3	0.56	0.86/0.57	−5.36	−3.16	−5.56	−2.73
4	0.54	0.86/0.61	−5.34	−3.16	−5.62	−2.81

[a] 150 °C in *o*-dichlorobenzene ($c = 10^{-4}$ M) with TBAHP ($c = 0.15$ M) as supporting electrolyte. [b] The HOMO and LUMO values were obtained in vacuum on the minimized structures at B3LYP/6-31G(d,p).

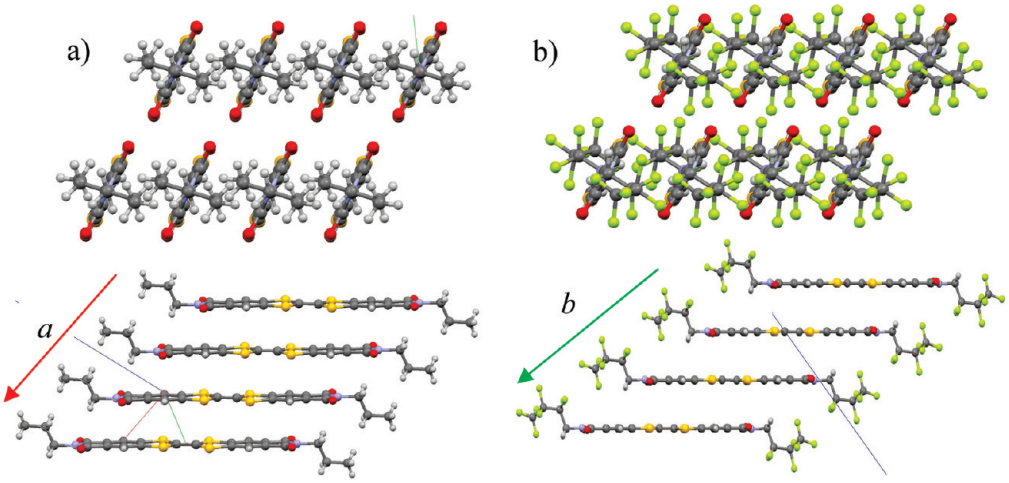

Figure 2. Different views of the columns formed in the crystal structures of compounds (a) **1** and (b) **3**.

The data obtained from CV and UV−vis permits the estimation of the frontier orbitals by means of the following equation: $E_{HOMO} = -e(4.8 + E_{1/2})$, considering the HOMO−LUMO gap as the energy corresponding to the onset of the most red-shifted absorbance band of the UV−vis spectra. The estimated HOMO energies are around −5.35 eV for compounds **2**, **3**, and **4**, while for **1** the value is higher, −5.27 eV. These values are still close to the gold work function but are lower than well-known TTF derivatives successfully employed for OFETs, such as DB-TTF ($E_{HOMO} = -4.88$ eV).[15] This indicates that the resulting materials are suitable for hole injection and, additionally, might exhibit higher air stability since it is well-known that a low lying HOMO hampers the material oxidation and even prevents structural or chemical changes caused by oxygen or water present in moisture.[44−46] Energy values of the LUMOs are around −3.15 eV for compounds **2**, **3**, and **4** and slightly higher (about 15 meV) for **1**, following the same trend found in the HOMO orbitals (Table 1). These LUMO values, though not low enough to allow an air stable operation of the devices in n-channel mode, should permit the electron injection from electrodes.

The energy of frontier orbitals was also estimated by DFT calculations. The structures were optimized at the B3LYP/6-31G(d,p) level in vacuum with Gaussian 09, and planar conformations were observed for all molecules. The computed HOMOs are in all cases placed in the TTF core, while LUMO orbitals are fundamentally situated in the phenyl and in the C═O groups of the phthalimide moiety. These values are collected in Table 1. The HOMO energy for **1** is −5.34 eV and for the other compounds of the family is slightly lower. The values of LUMO energies exhibit a similar tendency, being −2.45 eV for **1** but approximately 0.25 eV lower in the case of the fluorinated compounds **2**, **3**, and **4**. Although the calculated values are higher than the experimentally estimated ones, the tendency and relative increments between them are very similar.

XRD Characterization. High quality single crystals of **1** and **3** for XRD characterization were obtained by slow cooling a solution of the TTF derivative in *o*-dichlorobenzene from 180 °C to room temperature, which resulted in the crystallization of the materials as red plates at the air−solvent interface due to the lower temperature in this area. Relevant crystallographic data are reported in Table S1 (Supporting Information).

Both compounds crystallize in the triclinic system, space group $P\bar{1}$ with $Z = 1/2$. In **1** the molecules are essentially flat with the six rings coplanar and the propyl groups adopting a pseudo-trans configuration (Figure 2a). The molecules stack in a face-to-face mode forming columns along the *a* axis, where each unit is slightly displaced both longitudinally and transversally with respect to the nearest one and with an interplanar distance of 3.647 Å. The closest S···S (3.794 Å) and O···O (3.412 Å)

(44) Wang, J.; Liu, K.; Liu, Y.-Y.; Song, C.-L.; Shi, Z.-F.; Peng, J.-B.; Zhang, H.-L.; Cao, X.-P. *Org. Lett.* **2009**, *11*, 2563–2566.
(45) Wolak, M. A.; Jang, B. B.; Palilis, L. C.; Kafafi, Z. H. *J. Phys. Chem. B* **2004**, *108*, 5492–5499.
(46) Li, Y.; Wu, Y.; Liu, P.; Prostan, Z.; Gardner, S.; Ong, B. S. *Chem. Mater.* **2007**, *19*, 418–423.

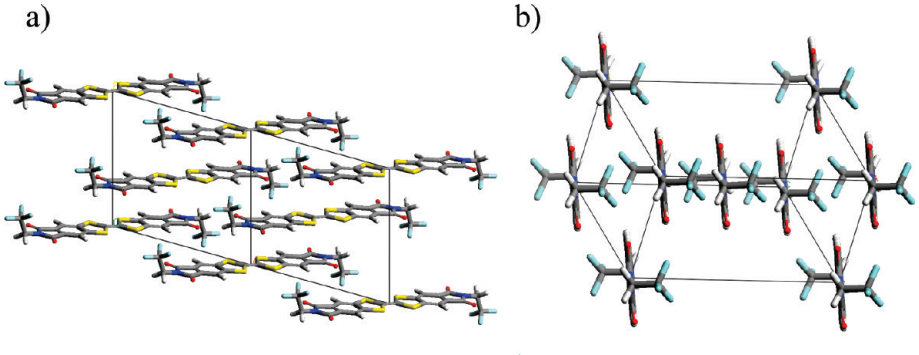

Figure 3. Crystal structures of compound **2** projected (a) in a plane perpendicular to the *c* axis and (b) in the plane perpendicular to the longitudinal axis of the molecules.

distances are, nevertheless, observed along the *b* axis. Lateral S···S (3.813 Å) and O···S (3.176 Å) contacts between molecules in the columns forming a plane are found. Indexation measurements show that the long dimension of the crystal corresponds to the *a* axis of the unit cell, which is the stacking direction.

In compound **3** the molecules are also flat, and the packing is quite similar to compound **1**; however, the *a* and *b* axes are inverted between the two structures for crystallographic conventions. The molecules in **3** stack forming columns along the *b* axis; in this case, molecules inside the stack are more displaced both longitudinally and transversally (Figure 2b). The shortest S···S (3.660 Å) and O···O (3.290 Å) contacts are found along the *a* axis, and lateral structure similar to that of **1** is observed. Indexation of the crystal has shown that the long side of the crystals corresponds to the *b* axis of the unit cell.

It is important to mention that both single crystal structures are representative of the bulk polycrystalline samples as checked by powder X-ray diffraction (see Supporting Information).

To gain a better understanding of the solid state structure of compounds **2** and **4**, high quality polycrystalline samples were prepared by recrystallization in *o*-dichlorobenzene at 180 °C. The powder diffraction patterns obtained from the recrystallized samples were used for structure determination using X-ray powder diffraction methods.[47−52] The Rietveld plots for the final fully refined models are reported in the Supporting Information.

Compound **4** crystallizes in the triclinic system, space group $P\bar{1}$, and has a very similar packing of that of compounds **1** and **3** (Figure S1 in Supporting Information). In contrast, the crystal structure of compound **2** presents a unit cell containing two crystallographically independent molecules with the center of symmetry of one molecule located at the inversion centers in special positions at (0,0,0) and (1/2, 1/2, 1/2). The six rings of the skeleton are coplanar and have the CF_3 residues adopting the *trans* configuration imposed by symmetry. The crystal packing is composed of layers of TTF molecules in which the aromatic rings of the molecules interact edge-to-edge through the $F_3C-C\cdots C-CF_3$ contact (4.198 Å) along the *a* axis direction. The stacking of layers results in columns of TTF molecules built along the *b* axis in which the TTF cores of a molecule are placed over the phthalimide moiety of the consecutive one. A projection in the *ab* plane is shown in Figure 3a.

Theoretical Characterization of Charge Transport Properties. Charge transport between two adjacent molecules is often characterized by a transfer rate which describes the hopping frequency going from a molecule M_1 initially charged to a neutral molecule M_2.[53] The expression of the charge transfer rate is defined in this case, in the context of Marcus−Levich−Jortner (M-L-J) theory:[54]

$$k_{hop} = \frac{2\pi}{\hbar} J^2 \sqrt{\frac{1}{4\pi\lambda_S k_B T}} \sum_{n=0}^{\infty} \exp(-S) \frac{S^n}{n!} \exp\left[-\frac{(\Delta G^0 + \lambda_S + n\hbar\omega_i)^2}{4\lambda_S k_B T}\right] \quad (1)$$

The charge transfer rate k_{hop} depends on several parameters. Among them, the transfer integrals J and internal reorganization energy λ_i are accessible from quantum-chemical calculations:

- J reflects the strength of the interactions between the electronic levels (HOMO for hole and LUMO for electron) of the molecules involved in the charge transfer process.[40,41]
- S is the Huang−Rhys factor associated to a single effective intramolecular vibrational mode (with a typical energy $\hbar\omega_i$ set here to 0.2 eV) that assists the charge transfer by allowing for tunneling across the energy barrier. S is directly related to the internal reorganization energy λ_i ($= S\cdot\hbar\omega_i$) that depicts the changes in the geometry of the two molecules during the electron transfer reaction $M_1^{+/-} + M_2 \rightarrow M_1 + M_2^{+/-}$.[55] λ_i is often computed at the DFT

(47) Giacovazzo, C. *Direct methods in Crystallography*; Academic Press: London, 1980.
(48) Harris, K. D. M.; Tremayne, M.; Kariuki, B. M. *Angew. Chem., Int. Ed.* **2001**, *40*, 1626–1651.
(49) Harris, K. D. M.; Cheung, E. Y. *Chem. Soc. Rev.* **2004**, *33*, 526–538.
(50) Harris, K. D. M.; Tremayne, M.; Lightfoot, P.; Bruce, P. G. *J. Am. Chem. Soc.* **1994**, *116*, 3543–3547.
(51) Harris, K. D. M. *Cryst. Growth Des.* **2003**, *3*, 887–895.
(52) David, W. I. F.; Shankland, K.; McCusker, L. B.; Baerlocher, C. *Structure Determination from Powder Diffraction Data*; Oxford University Press: Oxford, 2002.
(53) Troisi, A.; Orlandi, G. *Phys. Rev. Lett.* **2006**, *96*, 86601.
(54) Jortner, J. *J. Chem. Phys.* **1976**, *64*, 4860–4867.

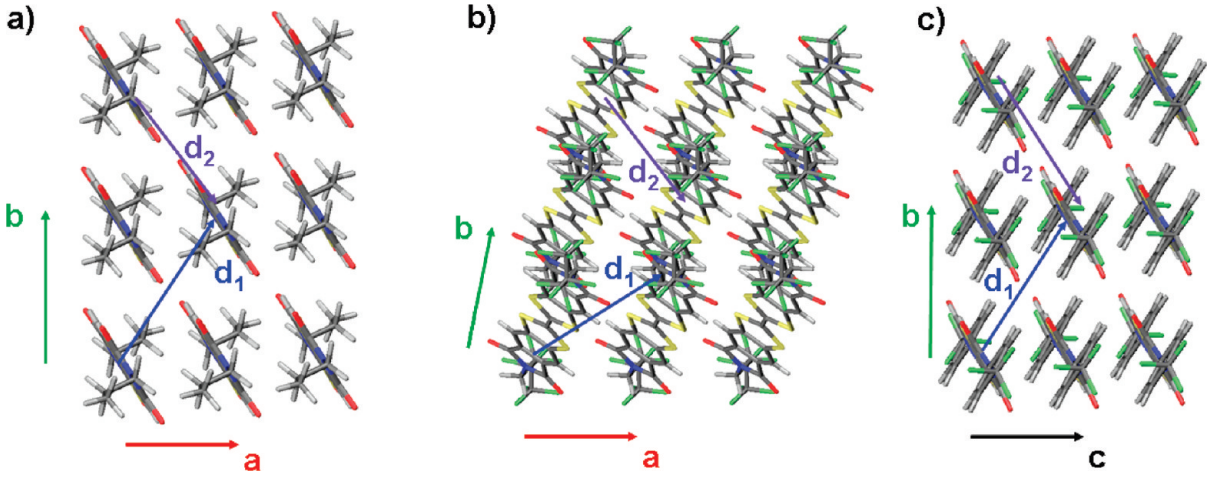

Figure 4. Crystalline motives considered for the calculations of the transfer integral as well as of the charge carrier mobilities for compounds **1**, **3**, and **4**.

Scheme 1

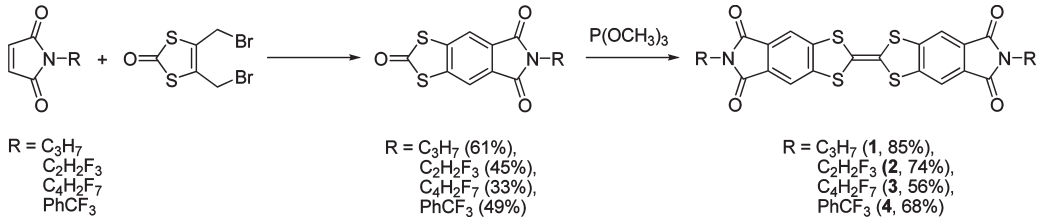

Table 2. Transfer Integrals Values for Hole and Electron Transport for the Different Directions of Compounds 1, 3, and 4 Crystalline Motives

	compound **1**		compound **3**		compound **4**	
direction[a]	J_{HOMO} (meV)	J_{LUMO} (meV)	J_{HOMO} (meV)	J_{LUMO} (meV)	J_{HOMO} (meV)	J_{LUMO} (meV)
a	27	8.1	97	41		
b	85.4	17.5	38	19	29.3	14.8
c					58.8	91.2
d_1	1.9	3.97	11	6	0.8	~0
d_2	7.5	3.2	0.4	0.5	12.4	5.4

[a] Relative direction of the pairs of molecules in the crystal defined in Figure 4.

level with the B3LYP functional and a 6-31G(d,p) basis set due to the good agreement observed with values extracted from ultraviolet photoemission spectroscopy spectra.[56]

- ΔG^0 is the Gibbs free energy which is related to the difference in energy between the configuration before and after the charge transfer. In the case of the single crystals, ΔG^0 reduces to the energy difference created by the presence of the electric field, namely, $\Delta G^0 = \pm e \cdot \vec{F} \cdot \vec{d}$. The ± sign is there to account for the nature of the charge carrier. Indeed, in absence of disorder, a hole (electron) experiences upward (downward) energy hops.

The Marcus expression shows that high transfer rates require a large transfer integral and small reorganization energy.

The calculations made in the previous section have revealed that the shape of the frontier orbitals was not changed upon substitutions. Moreover, the bond-length modification upon oxidation (reduction) shows that the main changes are systematically located over the TTF core (imide groups), leading to the appearance of a quinoid structure. For these reasons, we have neglected the external substituents to evaluate the reorganization energy and consider the derivatives from Scheme 1 with R≡H. As a consequence, the derivatives reported in this study are all characterized by the same reorganization energy for positive (negative) polaron. The internal reorganization energies are found to be 271 and 244 meV for positive and negative polarons, respectively. Interestingly, it appears that the internal reorganization energy for the positive polaron is quite similar to DB-TTF (250 meV). The addition of the imide groups seems to has a small impact on this parameter, most probably due to the localization of the HOMO orbital of the newly synthesized compounds on the TTF core. Note that such λ_i values are larger than that calculated at the same level of theory for pentacene (~100 meV).[57] However, a theoretical study on DT-TTF showed that when the local molecular environment is taken into account in DT-TTF

(55) Olivier, Y.; Muccioli, L.; Lemaur, V.; Geerts, Y. H.; Zannoni, C.; Cornil, J. *J. Phys. Chem. B* **2009**, *113*, 14102.
(56) Coropceanu, V.; Malagoli, M.; da Silva Filho, D. A.; Gruhn, N. E.; Bill, T. G.; Brédas, J. L. *Phys. Rev. Lett.* **2002**, *89*, 275503.

(i.e., including in the calculation a cluster of molecules instead of a single one) and the charge can be partially delocalized over several molecules, the value of the reorganization energy is reduced. This behavior can also be expected to take place in other TTF derivatives.[58,59]

Previous theoretical works[60−62] have shown that the magnitude of the transfer integral is driven by the shape of the molecular orbitals as well as by the relative position of the molecules involved in the charge transfer. We have thus calculated the electron and hole transfer integrals for all directions that present close contacts in the crystalline structures and have reported hereafter only the non-negligible contributions. Interestingly, compounds **1**, **3**, and **4** have quite similar structures, which should lead to a charge transport mainly limited to a plane of the crystal structure (*a*−*b* plane for **1** and **3**, *b*−*c* plane for **4**).

In Figure 4, we report the packing of the molecules considered for those three derivatives in the charge transport simulations. As previously described, the packings are quite similar; the main difference comes from the directions with the closest contact which are *b*, *a*, and *c* axes for compounds **1**, **3**, and **4**, respectively.

The calculations of the transfer integrals reveal that hole transport is largely favored along the direction with the shortest contact directions (namely, *b* and *a* axes for **1** and **3**, respectively) due to the tight packing along this axis. In the view of the transfer integral values, hole mobility is expected to be much higher than electron mobility in these structures, although in the case of compound **3** electron mobility is expected to be considerably larger than in compound **1**. Similarly as with previous molecules, **4** shows the largest transfer integral along the closest contact direction (namely, *c*). However, in this case, larger LUMO than HOMO transfer integrals are calculated, leading most probably to larger mobility for electrons than for holes.

Interestingly, the behavior of **2** is completely different than the molecules discussed previously. Indeed, it exhibits a three-dimensional charge transport pattern since pathways with non-negligible transfer integrals going to all crystallographic planes should be considered for the characterization of the charge mobilities. The largest HOMO (LUMO) transfer integral has been calculated at a value of 25.5 meV (41.1 meV) along direction d_2 (see Figure S15 and Table S2 in Supporting Information).

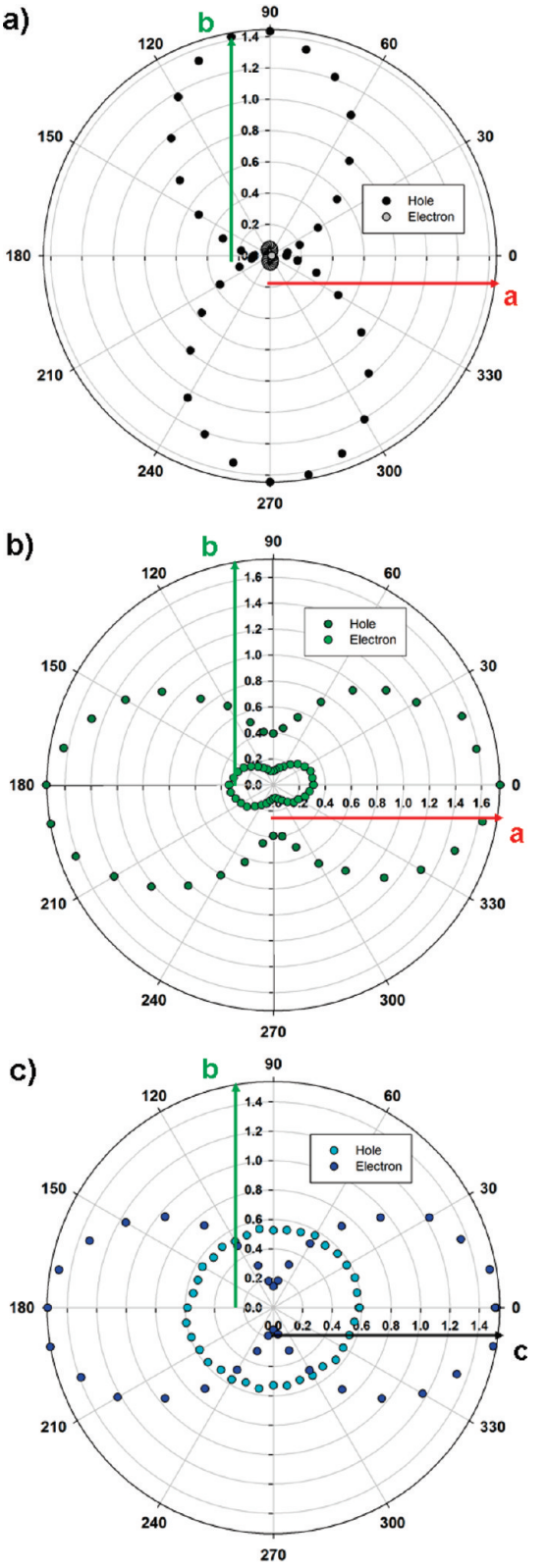

Figure 5. Anisotropy of hole and electron mobilities calculated for (a) **1**, (b) **3**, and (c) **4**.

Several experimental studies[63−65] have nicely shown that the charge carrier mobility in single crystals is generally not isotropic because of the high sensitivity of electronic couplings to molecular packing. Kinetic Monte

(57) Olivier, Y.; Lemaur, V.; Bredas, J. L.; Cornil, J. *J. Phys. Chem. A* **2006**, *110*, 6356.
(58) Bromley, S. T.; Mas-Torrent, M.; Hadley, P.; Rovira, C. *J. Am. Chem. Soc.* **2004**, *126*, 6544–6545.
(59) Bromley, S. T.; Illas, F.; Mas-Torrent, M. *Phys. Chem. Chem. Phys.* **2008**, *10*, 121–127.
(60) Lemaur, V.; da Silva Filho, D. A.; Coropceanu, V.; Lehmann, M.; Geerts, Y.; Piris, J.; Debije, M. G.; Craats, A. M. v. d.; Senthilkumar, K.; Siebbeles, L. D. A.; Warman, J. M.; Brédas, J. L.; Cornil, J. *J. Am. Chem. Soc.* **2004**, *126*, 3271–3279.
(61) Brédas, J. L.; Calbert, J. P.; Filho, D. A. d. S.; Cornil, J. *Proc. Natl. Acad. Sci. U.S.A.* **2002**, *99*, 5804–5809.
(62) Brédas, J. L.; Beljonne, D.; Coropceanu, V.; Cornil, J. *Chem. Rev.* **2004**, *104*, 4971–5004.
(63) Reese, C.; Bao, Z. *Adv. Mater.* **2007**, *19*, 4535–4538.
(64) Sundar, V. C.; Zaumseil, J.; Podzorov, V.; Menard, E.; Willett, R. L.; Someya, T.; Gershenson, M. E.; Rogers, J. A. *Science* **2004**, *303*, 1644–1646.
(65) Lee, J. Y.; Roth, S.; Park, Y. W. *Appl. Phys. Lett.* **2006**, *88*, 252106.

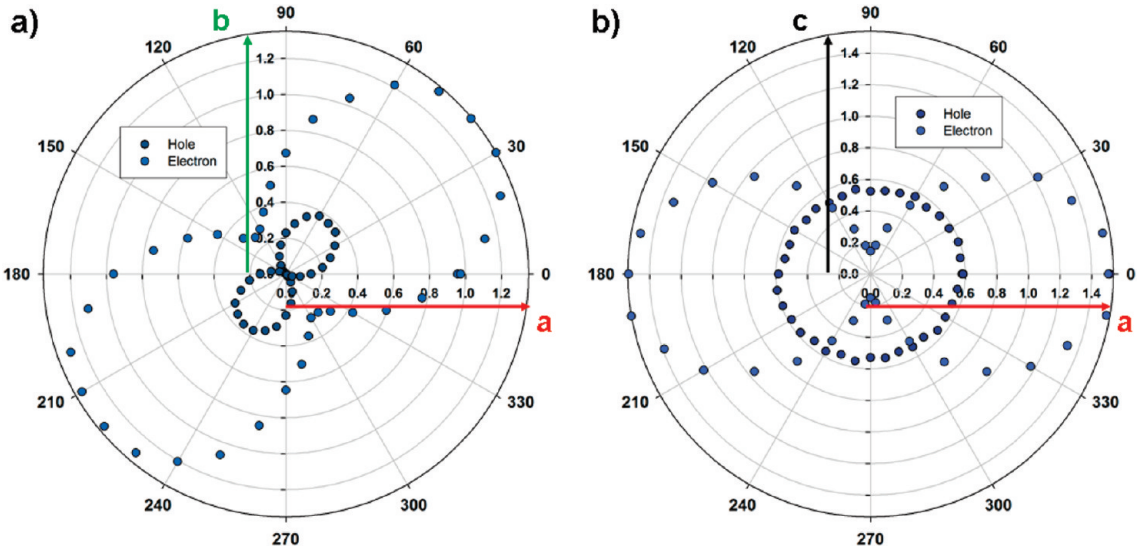

Figure 6. Anisotropy of hole and electron mobilities of compound **2** calculated (a) in the $a-b$ plane and (b) in the $a-c$ plane.

Carlo simulations have thus been performed to characterize the anisotropy of both hole and electron mobilities for the different TTF derivatives.

Hole (electron) mobilities in derivatives **1**, **3**, and **4** have their largest value along the directions where shortest contact between adjacent molecules and maximum transfer integrals are found, namely, b (for **1**), a axis (for **3**), and c axis (for **4**). The magnitude of the hole mobility for compounds **1** and **3** along these directions is comparable because of the similar transfer integrals values. The ratios of the mobilities along b (a) and a (b) are around 14 and 3.5 for **1** and **3**. The reason for the difference between the two derivatives comes from the larger contribution of the d_1 axis in **3** (Figure 5a,b). From the transfer integral calculations, the electron mobilities for those derivatives are expected to be smaller than the hole mobilities and are actually lower by more than 1 order of magnitude and by a factor of 5 for **1** and **3**, respectively (Figure 5a,b, zoom of the electron mobility of **1**, Figure S13 in Supporting Information). The orientation of the anisotropy is similar for both hole and electron mobilities, which is not surprising in view of the transfer integral values. It is worth mentioning that the difference in charge carrier mobilities is due to the difference in transfer integral values since internal reorganization energies are quite similar.

Interestingly, compound **4** exhibits completely opposite behavior compared to the previous molecules. Electron mobility is larger than hole mobility. The anisotropy as well as the magnitude of the electron mobility is reminiscent of the behavior of the hole mobility of **3**, which again, is not surprising when looking at the most important transfer integral contributions. However, the magnitude of the electron mobility of **4** along b (0.14 $cm^2 V^{-1} s^{-1}$) is lower than the hole mobility of **3** (0.39 $cm^2 V^{-1} s^{-1}$), which is explained by the lower values of the transfer integrals along b and the diagonal directions.

To highlight the three-dimensional nature of charge transport in compound **2**, we have calculated the anisotropy in the mobility for each charge carrier in the $a-b$ plane and in the $a-c$ plane. As seen in Figure 6, the maximum hole and electron mobilities are comparable, the orientation of the hole and electron mobility being rotated by 40° with respect to a axis in the $a-b$ plane calculations. It is always difficult to comment on the orientation of the anisotropy curves, but we can say with good confidence that the positions of the mobility maxima are observed for orientations that optimized the charge transport along the diagonal directions, namely, along d_2 and d_3 (see Figures S14 and S15 and Table S2 in Supporting Information). We notice that the electron mobility is larger than the hole mobility because of the magnitude of the transfer integral. Moreover, the maximum hole and electron mobility magnitudes of **2** and **4** are about the same.

Table 3. Electrical ToF Mobilities of Compounds 1−4

compound	p-type mobilities ($cm^2 V^{-1} s^{-1}$)	n-type mobilities ($cm^2 V^{-1} s^{-1}$)
1	0.11	0.06
2	3.6 ± 0.1 ($\times 10^{-6}$)	3.4 ± 0.1 ($\times 10^{-6}$)
3, powder	[a]	0.3 ± 0.15
3, crystal	2.1 ± 0.1	1.6 ± 0.13
4	1 ± 1.5 ($\times 10^{-6}$)	2.5 ± 0.1 ($\times 10^{-6}$)

[a] Estimation of p-type mobility was not possible due to very low device currents.

All the previously commented results predict that compounds **1**−**4** should behave as p-type and n-type semiconductors, although it is well-known that electron injection problems might arise in devices based on semiconductors that have a LUMO energy above −3.5 eV.[66−69]

(66) Tang, M. L.; Reichardt, A. D.; Wei, P.; Bao, Z. *J. Am. Chem. Soc.* **2009**, *131*, 5264–5273.
(67) Marrocchi, A.; Seri, M.; Kim, C.; Facchetti, A.; Taticchi, A.; Marks, T. J. *Chem. Mater.* **2009**, *21*, 2592–2594.
(68) Ortiz, R. P.; Facchetti, A.; Marks, T. J.; Casado, J.; Zgierski, M. Z.; Kozaki, M.; Hernandez, V.; Navarrete, J. T. L. *Adv. Funct. Mater.* **2009**, *19*, 386–394.
(69) Piliego, C.; Jarzab, D.; Gigli, G.; Chen, Z.; Facchetti, A.; Loi, M. A. *Adv. Mater.* **2009**, *21*, 1573–1576.

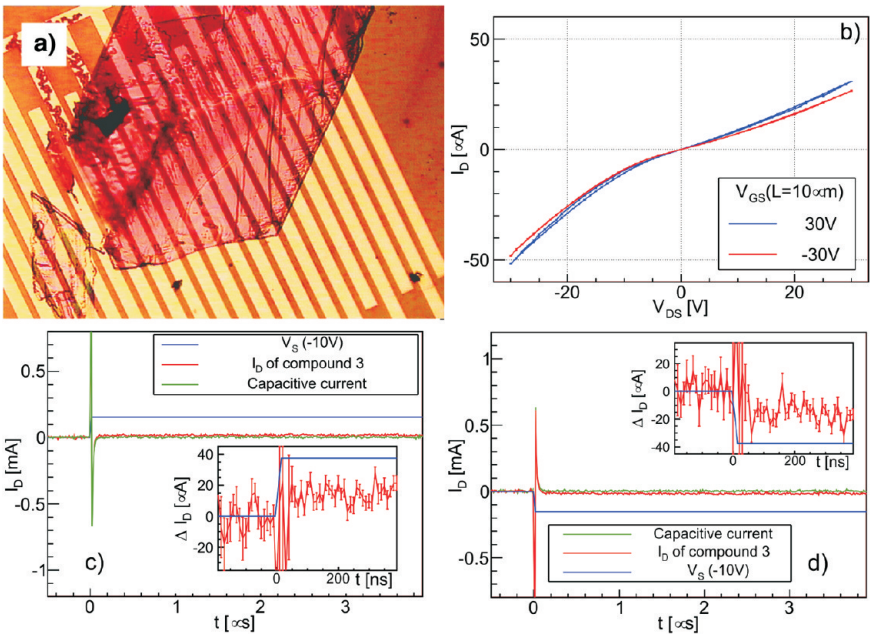

Figure 7. a) Optical microscope image of the measured crystal of compound **3**. b) Current−voltage characteristics of a measured device. c) Electrical time-of-flight measurement for p-type charge carriers. d) Electrical time-of-flight measurement for n-type charge carriers. The leakage current is presented as an error bar in current−voltage graphs.

Charge Transport Measurements. The intrinsic charge carrier mobility of all compounds has been investigated by electrical time of flight (EToF) measurements. The EToF measurements were performed with samples of the TTF derivatives in a microcrystalline form, and compound **3** was also measured as a single crystal. When polycrystalline samples were used, the organic semiconductors did not cover completely the channel surface (see Supporting Information), and as a result, the measured drain current was relatively low compared to the capacitive current, which is also measured, and arises due to capacitive coupling between the drain, source, and gate electrodes. To obtain the contribution of the capacitive coupling, we have measured a sample with no organic semiconductor using the same experimental setup. Capacitive current was subtracted from the measured drain current of a transistor with organic semiconductor. The resulting current, which is flowing through the organic semiconductor, is presented as ΔI_D. Table 3 gathers the charge transport data.

Compounds **1** and **3** form flat rod-like crystals which are a few micrometers in size (see Supporting Information). The current−voltage dependence presents relatively unstable output characteristics. In general, the negative gate voltage is resulting in higher drain current, comparing to the positive gate voltage. In the case of compound **1**, the current is turned on only after the drain-source voltage is above a threshold voltage of 2 V for negative gate voltage and above 8 V for positive voltage. This indicates that the electron injection from Au contacts is less efficient, relative to hole injection. In this compound, as well as in other compounds of the family, a relatively poor dependence on the gate voltage has been observed. This suggests a poor contact between the organic semiconductor and the dielectric. On the other hand, we have obtained a reliable measurement of the derivative **3** in a single crystal form (Figure 7). No leakage current through the gate electrode was observed, and p-type and n-type mobilities as high as 2.1 ± 0.1 cm^2 V^{-1} s^{-1} and 1.6 ± 0.13 cm^2 V^{-1} s^{-1}, respectively, were measured.

For compounds **2** and **4**, which form much smaller crystals than compound **1** or **3**, the current−voltage characteristics exhibit a relatively low current, comparable to the leakage current. This is likely due to the relatively low number of interconnected crystals. Charge carrier mobilities for both compounds are very similar (Table 3) even though their crystal structures are different.

Single crystal OFETs of **1** were successfully fabricated by growing the crystal from solution on a Si/SiO_2 substrate and painting with graphite paste the source and drain electrodes. The presence of cracks along and across the crystal was clearly observable, which was attributed to the stress induced during the crystallization since this process was carried out at high temperature ($T \sim 110$ °C).

A typical output and transfer characteristics are shown in Figure 8. The device behaves as a p-type material since the source−drain current increases with negative gate voltage. We should mention that at low source−drain voltages the contact was not ideal in this device, but this effect was even more pronounced when gold was used as source and drain contacts. From the transfer characteristics in the saturation regime a high hole mobility of 0.33 cm^2 V^{-1} s^{-1} was extracted. The rather high threshold voltages found for this device indicate a high level of charge trapping due to the crystal cracks or to interface problems with the dielectric. Typical on/off current ratios of about $\sim 10^2$ were found.

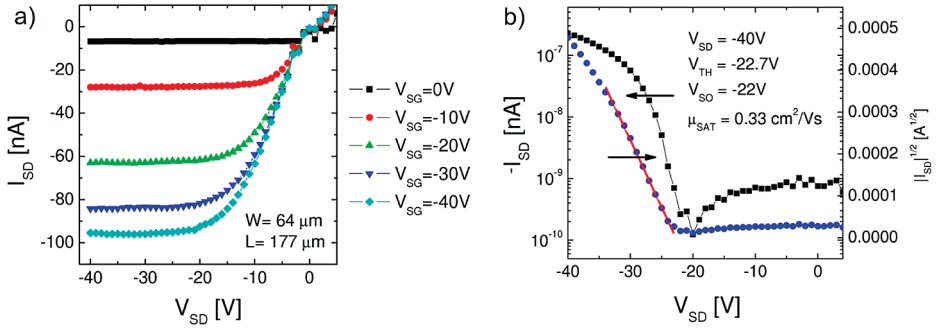

Figure 8. (a) Output characteristics of a single crystal of compound **1** based OFET using graphite source and drain electrodes. (b) Semilogarithmic transfer characteristics and extraction of field effect mobility in the saturation regime.

It is worth mentioning that this low on/off current ratio is related to the low W/L ratio of the crystals as well as the current sensitivity limitation of the source-meter used. No electron mobility was detected in these devices when applying positive gate voltages. To test the stability of the transistors, they were measured 5 weeks after being stored at room temperature in air, and no decrease of the mobility was observed.

Attempts to fabricate thin-film devices were also carried out. However, evaporation of the compounds **1**−**4** employing a variety of conditions (substrate temperature, evaporation rates, type of substrates, etc.) resulted always in the growth of columns that were not well-connected. Therefore, no field-effect mobility could be measured in these films.

Summary

We have described the synthesis and characterization of a series of *bis*-phthalimide tetrathiafulvalenes substituted with different side chains as potential ambipolar semiconductors. The electron-withdrawing groups contribute to reduce the energies of frontier orbitals, making the prepared devices air stable, and also allows for improved electron injection and transport as it has been shown in the EToF measurements. Crystal structures of all compounds have been resolved by X-ray spectroscopy. With the solid state structure and the theoretical calculations carried out, we have studied the capabilities of these materials for their use as semiconductors with hole and electron conduction. DFT quantum-chemical calculations have been used to calculate the reorganization energy and electronic coupling to establish the probability of charge hopping. Moreover, the anisotropy and the magnitude of the mobilities in the crystals have been studied. This study establishes that the crystals are excellent both for hole and electron conduction with anisotropic charge transport. Electrical time-of-flight measurements have shown mobilities up to 2.1 $cm^2\ V^{-1}\ s^{-1}$ for holes and 1.6 $cm^2\ V^{-1}\ s^{-1}$ for electrons for a single crystal of **3**. OFETs from compound **1** were also fabricated with single crystals, and a high performance and stability has been observed with hole mobility on the order of 0.33 $cm^2\ V^{-1}\ s^{-1}$. These studies conclude that attaching electron-withdrawing groups to TTF, a well-known p-type organic semiconductor, is a suitable approach to increase the stability of the devices and can lead to the preparation of novel ambipolar materials, which are essential to develop in order to progress in the field of organic devices.

Acknowledgment. The research leading to these results has received funding from the European Community's Seventh Framework Programme (FP7/2007-2013) under grant agreement no. 212311 of the ONE-P project, Marie Curie EST FuMASSEC, DGI, Spain (contracts CTQ2006-06333/BQU and CTQ2010-195011/BQU), the Generalitat de Catalunya (2009SGR00516), and the program "Juan de la Cierva" (MICINN). We also thank Stefan T. Bromley for his advice regarding the DFT calculations and CESGA for the use of their computational resources. The work in Mons is also supported by the European ONE-P project as well as by the Belgian National Fund for Scientific Research (FNRS). Y.O. and J.C. are FNRS research fellows.

Supporting Information Available: Electrochemical, UV−vis, and XRD data. Description of EToF technique and more theoretical results are also shown (PDF). This material is available free of charge via the Internet at http://pubs.acs.org.